



A proposed method for enhancing the thermal characteristics of bio-inspired microtextured surfaces for energy sector applications

Haydee Martinez-Zavala¹ · Debajyoti Bhaduri¹ · Mohamed Al-fahham² · Agustin Valera-Medina¹ · Samuel Bigot¹

Received: 29 January 2025 / Accepted: 10 April 2025
© The Author(s) 2025

Abstract

The research involves generation of textured surfaces using micro-wire electro discharge machining (μ -WEDM) for controlling boundary layers, drag force and heat transfer during fluid flow over the textured surfaces. Numerical analysis of the drag experienced by air, flowing over the microtextured surfaces, is initially carried out using a Large Eddy Simulation (LES) open-source code, Hydro3D, by simulating turbulent flow over the textured surfaces. This is then followed by the manufacture of four microtexture geometries on stainless steel specimens via μ -WEDM and their characterisation using a 3D optical profiler. Velocity profile experiments are then carried out on the micro-geometries at different angles of action against the air flow direction to analyse drag reduction and boundary layer thickness. And finally, heat transfer experiments are carried out in a condensation chamber to evaluate surface temperature differential (ΔT_s) during matter's phase change. The results demonstrate that the numerical approach is reliable to simulate air flow over the microtextured surfaces when solving Navier–Stokes equations. The velocity profile experiments exhibit lower drag force (by 6.9–16.9%) on the microtextured surfaces as a result of the wall shear stress and boundary layer thickness diminution. The textured surfaces further aid in enhancing the heat transfer during condensation, due to 8.6–25.7% higher surface temperature differentials (ΔT_s), heat fluxes (q) and condensation heat transfer coefficients (h), when compared to the untextured surfaces.

Keywords Biomimetics · Texturing · Wire-EDM · Condensation · Drag · Boundary layer

Highlights

- Bio-inspired microtextured surfaces represent a passive mechanism on surface topographical modification for energy applications.
- Bio-inspired microtextured surfaces are successfully manufactured via micro-wire electro discharge machining (μ -WEDM).
- The Large Eddy Simulation (LES) model is capable of simulating turbulent flows over microtextured surfaces.
- Microtextured surfaces experimentally achieve 6.9–16.9% drag reduction and 5.7–12.6% boundary layer thickness reduction in turbulent flows.
- Microtextured surfaces exhibit 8.6–25.7% higher surface temperature differentials (ΔT_s), heat fluxes (q) and condensation heat transfer coefficients (h), compared to the untextured surfaces.

✉ Debajyoti Bhaduri
BhaduriD@cardiff.ac.uk; debajyoti.bhaduri@gmail.com

¹ School of Engineering, Cardiff University, Queen's Buildings, The Parade, Cardiff CF24 3AA, UK

² Aeronautical Engineering, Engineering Technical College-Najaf, Al-Furat Al-Awsat Technical University, 31001 Al-Kufa, Iraq

1 Introduction

1.1 Background to the research

From macro to micro and nanoscale, evolution and adaptation of species to the environment have inspired researchers to introduce bespoke and innovative solutions to complex engineering problems. By understanding the surface properties of natural species, biomimetic engineering can lead to developing novel engineered materials with efficiently custom-made surface characteristics that can imitate physicochemical properties of plants and animals with prominent commercial and industrial interest in areas such as thermal engineering, fluid mechanics, transportation, electrical, electronics, construction, sportswear and biomedical sectors for energy recovery, reduced energy consumption, thermal and vehicle stabilisation, anti-fouling and surface self-cleaning [1]. Some examples of these are the enrichment of aerodynamic lift in birds through their feather structures, high mechanical strengths of seashells, thermal insulation properties of mammal furs and skins and so on.

Other examples include super hydrophobicity of lotus leaves that facilitates self-cleaning and drag reduction leading to easy draining of water droplets while cleaning the surface to aid photosynthesis. The microscales or dermal denticles on sharkskin promotes cleanliness and lower drag force, thus allowing faster swimming capability of the species [2].

Low hydrodynamic drag and self-cleaning properties can potentially enhance the performance of energy recovery systems by improving heat transfer during matter's phase change and controlling the boundary layer for drag reduction. This can be achieved by adjusting surface roughness and/or chemistry through topographical modification (microtextures) and/or chemical modification (coatings). Chemical modification has been widely explored in both academia and industry since the 1950 s [3]. However, coatings have to be continuously replaced due to the reduction of their effectiveness and durability over time, and thus, the technology appears to be more expensive than topographical modification [4]. Therefore, surface engineering via microtexturing is a more reliable and cost-effective method for improving the surface characteristics through passive mechanisms. Various surface texturing methods have been explored comprehensively for different application areas. For example, Orazi et al. [5] employed a fast laser induced periodic surface structuring (LIPSS) method to create dental implants with complex geometries without any need of specific part programmes and use of expensive 5-axis, high precision manipulator systems. A simple and fast surface texturing technique by using nanosecond pulsed lasers has been demonstrated by Tran and Chun [6] to generate superhydrophobic surfaces. Surface texturing has also been extensively studied for developing structured cutting tools to enhance the tool life and cutting performance [7].

The use of nature-inspired microtextures for energy sector applications is still under development [8]. For example, the effects of the bio-inspired surfaces on the velocity and temperature fields of droplets/fluids have been investigated by Yu et al. [9] and Zhang et al. [10]. The condensation phenomenon has been widely utilised in chemical and environmental engineering processes, refrigeration and power generation sectors [11], because it can promote high convective heat transfer coefficients, while controlling the hydrodynamic drag has helped to optimise combustion systems performance [12]. The condensation phenomenon and hydrodynamic drag depend largely on the surface characteristics [4]. On untextured surfaces, it mainly depends on the nature of the fluid, the ambient conditions, the liquid–gas surface tension and surface energy; while on microtextured surfaces, their physical structure and the chemical heterogeneities also play a major role [13]. Compared to the basic surface texture designs, such as circles, triangles, lines, squares and cross-hatch, biomimetic microtextured surfaces can assist in greater heat transfer during condensation by

transferring energy from the large latent heat, associated with matter's phase change, to the surface of the device, instead of passing it to the drier air in energy systems, such as a heat exchanger. Additionally, microtextured surfaces can also reduce blow-off and flashback phenomena in combustion systems [12]. These phenomena are based on the generation of micro-vortical motion encapsulated in solid valleys, which, due to rotation, sustains a continuous exchange of energy while maintaining a single point-in-contact with the solid surface and thereby reduces drag and pressure losses [14]. This represents a novel cornerstone for the design of energy and combustion systems.

1.2 Aim and objectives

The enhancement of condensation heat transfer and drag reduction can be achieved through the modification of physicochemical properties of the surface [15]. This research aims to explore an alternative passive mechanism by surface topographical modification, in particular, via bio-inspired surface microtexturing. The objectives of the study were fulfilled through the following stages (also shown in Fig. 1):

1. Numerical simulation of different microtexture geometries via computational fluid dynamics (CFD) for drag reduction.
2. Based on the CFD analysis, manufacture and characterisation of four different bio-inspired micro-geometries, viz. Lotus, Scallop, Sharkskin and Diamond textures using μ -WEDM.
3. Velocity profile experiments for boundary layer control, drag reduction and angle of action against the flow direction.
4. Heat transfer experiments during condensation to assess the change in the surface temperature differential (ΔT_s), heat flux (q) and heat transfer coefficients (h).

2 Numerical analysis

2.1 Background

Initial numerical studies in the late 1980 s were performed by Bechert and Bartenwerfer [16] using conformal mapping to simulate the viscous sublayer of a turbulent boundary layer on a surface with fine longitudinal riblets. The velocity distribution over the various geometries was calculated. As a result, direct numerical simulation (DNS) has been widely used to simulate turbulent flows over textured surfaces as a physical method for drag reduction. In 1993, Chu and Karniadakis [17] used DNS to simulate a channel flow over textures (riblets) using a spectral element Fourier method. They found that the riblets limited the spanwise motion of

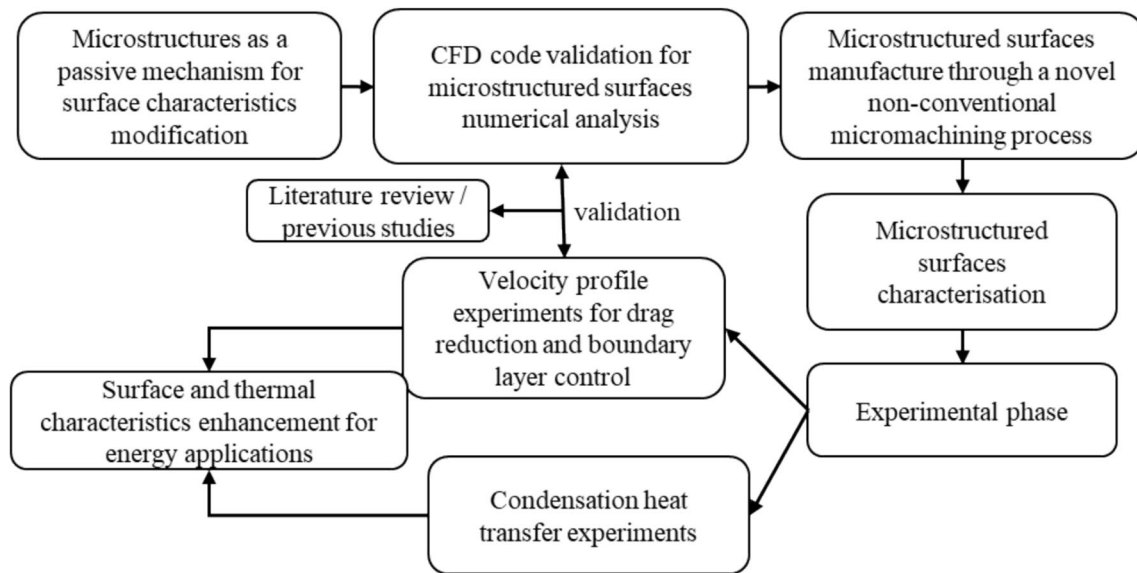


Fig. 1 Stages of the study

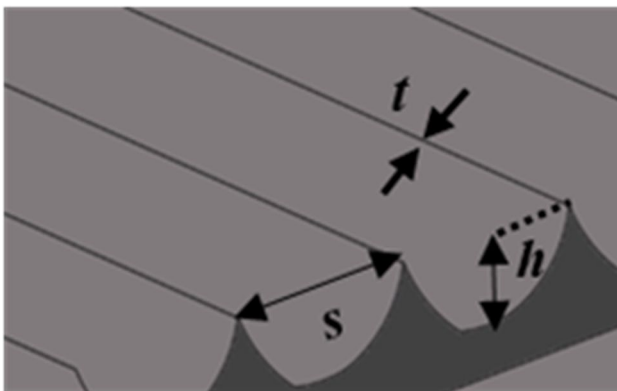


Fig. 2 Riblet parameters for numerical simulations

low-speed wall streaks, resulting in 6% drag reduction when compared to the flat surfaces. In order to compare the results, it is essential to identify the following wall unit parameters: $s^+ = su_\tau/v$, $h^+ = hu_\tau/v$ and $t^+ = tu_\tau/v$ where s , h , t , u_τ and v denote riblet space, riblet height, riblet thickness, friction velocity and kinematic viscosity, respectively. The parameters s , h and t are shown in Fig. 2. Haecheon [18] simulated turbulent flows over V-shaped riblet surfaces with $s^+ = 20$ and $s^+ = 40$, which exhibited a drag reduction of 5% and 6%. In addition, mean-velocity profiles were computed based on the virtual origin of the wall showing upward and downward shifts in the log-law for drag-decreasing and drag-increasing cases, respectively. Furthermore, Haecheon [18] suggested that the transverse flow near the wall was obstructed by the riblets due to the reduction of spanwise velocity fluctuations above the riblets, which occurred by the decrease of

the velocity and fluctuations of the vortices, as well as the Reynolds shear stress above the riblets.

Goldstein [19] used an immersed boundary technique to model a riblet-covered surface on one wall of a channel with fully developed turbulent flow. Results showed that the damping of cross-flow velocity fluctuations reduces drag. Very short riblets do not protrude far enough into the flow to sufficiently damp the kinematic viscosity fluctuations. Larger riblets, s^+ and h^+ in the range of 10 to 20, reduce the kinematic viscosity and have a lower drag in the valleys than that near the riblets peaks.

El-Samni et al. [20] investigated the effect of longitudinal thin rectangular riblets aligned with the flow direction on turbulent channel flows using DNS. They built the model using an immersed boundary method technique and tested different spacings between 11 and 43 wall units while keeping the height/space ratio at 0.5 and the Reynolds number at 150 based on the shear velocity and half channel width. They reported that 17 wall units are the optimum space corresponding to the maximum drag reduction.

DNS was used to investigate the drag reduction based on a scan of real biological sharkskin. It was found that the velocity rapidly changed from a high value on the tip to the negative velocity in the valleys (backflow). Also, the turbulence intensity was much larger on the tip than that on the valley, and the spreading movement of the vorticity was restricted by the grooves of the sharkskin, which led to drag reduction [21]. More importantly, Jin and Herwig [22] investigated drag reduction and heat transfer behaviour in channels with sharkskin surfaces using the DNS method. They analysed the turbulence close to the wall and concluded that certain turbulent structures are lifted off and

rearranged; hence, they proposed a mechanism called lift off and alignment (LOA), to support the results by analysing entropy generation rates.

Other models have also been assessed. Benhalilou and Kasagi [23] used a nonlinear low-Reynolds number $k-\epsilon$ model with several turbulent scalar flux representations to numerically study heat and momentum transfer characteristics in a fully developed turbulent channel flow with triangular riblets. The major advantages of the turbulence model they adopted are the elimination of the reference to the wall topography and the implementation of the shear parameters in the model function, which, combined with Reynold number, could be more useful in capturing the complex flow over the riblets.

Martin and Bhushan [24] used computational fluid dynamics (CFD) software package ANSYS Fluent 16.0 and Large Eddy Simulation (LES) model to investigate the optimal design of riblets through studying: spacing, height, thickness, gap and offset. They reported that the optimum spacing should be 15–20 wall units to lift away the vortices with 20–30 non-dimensional units, and the height should be around 8–10 wall units to minimise drag. However, thinner riblets are better as drag accrues at the riblet peaks. They numerically investigated three different riblet shapes with optimum parameters based on their previous work, i.e. $s^+ = 15\text{--}20$, $h^+ = 8\text{--}10$ and small t^+ . It was found that blade riblets had the greatest drag reduction by $\sim 11.6\%$, followed by that of the scalloped and saw shapes (by 5.7% and 4.1% drag reduction, respectively).

In summary, direct numerical simulations (DNS) is the preferable method in drag reduction modelling over surface structures or riblets due to its ability to solve the Navier–Stokes equation without any averaging closure or the need for a subgrid-scale model and to produce a series of non-empirical solutions. This method can address basic research questions regarding turbulence physics; however, the limitations of its computational cost, especially with high Reynolds numbers, prevent DNS's use as a general-purpose design tool, which can be challenging for microtextures' design. Therefore, an alternative modelling method that can solve the large scales of the flow field and filter out the small scales based on the turbulence criteria is Large Eddy Simulation (LES).

2.2 Methodology

For this study, a Large Eddy Simulation (LES) model, Hydro3D, was employed. The code was developed to solve the filtered Navier–Stokes equation on a Cartesian, block structure grid using the finite volume method [25]. This mathematical code for turbulence utilises the Immersed Boundary Method (IBM) to simplify problems relating to the grid around the object being modelled and can also

adopt different turbulent models such as Smagorinsky, wall-adapting local eddy-viscosity (WALE) model and the one-equation model. Moreover, Hydro3D allows parallelisation and local mesh refinement (LMR) in which the code can refine the mesh to concentrate the computing effort on the most important parts of the domain. The code has been validated via complex flow studies ranging from tidal turbines [26] to bubble plumes [27]. The governing equations used in Hydro3D are the spatially filtered Navier–Stokes equation for turbulent, incompressible, three-dimensional flow field, as depicted in Eqs. 1 and 2 [28].

$$\frac{\partial u_i}{\partial x_i} = 0 \quad (1)$$

$$\frac{\partial u_i}{\partial t} + \frac{\partial(u_i u_j)}{\partial x_j} = -\frac{\partial p}{\partial x_i} + \frac{1}{Re} \frac{\partial^2 u_i}{\partial x_i \partial x_j} - \frac{\partial \tau_{ij}}{\partial x_j} \quad (2)$$

where x_i and x_j are the spatial location vectors (i.e. x_i and $x_j = x, y, z$ for i and $j = 1, 2, 3$); u_i, u_j ($i, j = 1, 2, 3$) are the resolved velocity components in x -, y - and z -directions, respectively, normalised by the velocity U ; and p is the resolved pressure divided by the density. $Re = UL/\nu$ is the Reynolds number, where ν is the kinematic viscosity and L is the reference length scale [12, 28].

2.2.1 Wall-adapting local eddy viscosity (WALE)

In LES for incompressible flows, large-scale eddies are retained and directly solved by a transient solution. Meanwhile, the small eddies, which are smaller than the grid size, are removed and modelled using a subgrid scale (SGS) model. Most subgrid scale models are based on an eddy viscosity assumption of modelling the subgrid tensor [29]. In this work, the WALE model was used to model the small-scale fluctuations. WALE is a model in which the subgrid viscosity dynamically worked out with the square of the velocity gradient tensor rather than resolved through strain rate in a Smagorinsky-type model. This velocity tensor does not only account for the effects of both strain and rotation rate of the smallest resolved turbulence fluctuations but also recovers the proper near-wall scaling for the eddy viscosity without requiring a dynamic procedure. The model coefficient is proven to have a relatively constant value ($C_w^2/C_s^2 \approx 10\text{--}12$) [29]. Further, the WALE model is invariant to any coordinate translation or rotation, and no test-filtering operation is needed [12, 30]. This ensures the model's ability to calculate zero eddy viscosity in laminar shear flows automatically. The eddy viscosity calculation and the method to couple the pressure and velocity and to solve Poisson's equation using fourth-order accurate approximations are fully explained in [28]. It is essential to point out that Hydro3D

uses parallelised domain decomposition, dividing the computational domain into smaller sub-domains.

2.2.2 Local mesh refinement (LMR)

In the present work, the computational meshed domain was performed in three levels, from a coarse to a fine mesh. A 2:1 reduction in mesh size between neighbouring levels was performed on the staggered computational grid to implement LMR in critical areas of the geometries. The ghost cell method was used to ensure the accuracy of the pressure and velocity values in the interface between the coarse and fine meshes. For pressure, first, the values at the coarse computational grid cells are quadratically interpolated. Then, another quadratic interpolation is applied to calculate the fine ghost pressure. The edge-centre of the fine grids is calculated, and the arithmetic average of the fine-grid pressure is taken as the coarse grid pressure gradient to enforce the continuity of the gradient across the interface. For velocity, the case is slightly more complicated since the calculation and interpolation should be done for the tangential and normal velocities [12]. Full details of the procedure are well covered by Cevheri et al. in [28].

2.2.3 Computational domain and boundary conditions

The computational domain represents a fully developed turbulent flow inside a channel over a patch of microtextures on the lower wall aligned with the direction of the flow. No-slip condition was assigned to the bottom boundary of the computational domain. A slip condition was assigned to the upper and lateral boundaries to eliminate the wall effect of the flow over the studied area of the duct. To satisfy the physical boundary of this case, the inflow was established as a fully developed turbulent flow by running the computation for approximately 8 convective time units ($t = u_\tau / \delta$), where u_τ is the friction velocity and δ is the half channel height, using a periodic condition in inflow to ensure a fully developed turbulent flow. Then the resultant velocity profile was stored in an output file to use it as a pre-set velocity input for the next run. The Reynolds number was calculated based on δ and bulk velocity. For the comparison and verification of the code, the Reynolds number was varied from 2500 to 14,500, which is close to the values used by Martin and Bhushan [31]. In the streamwise direction (along the x-axis), the computational domain span is 10δ and the cross-sectional span (y-axis) is $\approx 3.3\delta$ with the wall-normal direction (z-axis) being 2δ . Because Hydro3D is an MPI-parallelisation code and LMR was employed, the main computational domain was divided into 36 smaller sub-domains into three levels of refinement. LMR was applied to these sub-domains on bases of 1:2 moving from a coarse mesh for

domains far from the wall to a finer mesh in domains at the vicinity of the wall.

2.2.4 Microtextured surface model

The microtexture geometries, riblets, were imposed in a small part of the computational domain to further study the flow before, over and behind the riblets. In terms of drag reduction and the validation of the code, as a first step, the simplest micro-geometries, blade riblets, were numerically tested with three different s^+ / h^+ ratios using two of the many advanced tools available in Hydro3D, i.e. the WALE model and the LMR to achieve the near-wall flow and also to save the computational time. The riblet height was kept constant for the three models at $h = 200 \mu\text{m}$ in order to have a non-dimensional height of ~ 10 as studied by Martin and Bhushan [24] for optimum drag reduction. Additionally, the blade thickness was kept minimum at $t = 12.5 \mu\text{m}$, as the thickness plays a significant role in drag reduction. The space between riblets (s^+) was also varied to be compared with the optimum s^+ results reported by Bixler and Bhushan [32]. Hence, the two approaches used for validation are as follows: (a) Changing bulk velocity with constant $h/s = 0.5$. This led to a change in the shear velocity and s^+ . Since the majority of recent research pointed out that the optimum drag reduction can be obtained from riblets that have s^+ ranging from 15 to 20 [33], the target was to investigate ranges of s^+ between 10 and 50 to cover all ranges and to test new designs. (b) Changing space between blade riblets, three common ratios of h/s were chosen: 0.5, 0.8 and 1. Table 1 shows a summary of the parameters used in each case for the code validation.

After validating the code with these parameters as well as based on the available literature, four microtexture geometries were analysed in the computational domain from Fig. 3, manufactured, characterised and experimentally evaluated. These were as follows: a geometry based on the lotus leaves (Lotus); a simpler design of the lotus leaf geometry (Scallop); a geometry based on sharkskin (Sharkskin); and a simpler version of sharkskin (Diamond), adopted from the authors' prior work [34], and shown in Fig. 4.

3 Manufacture and characterisation of the microtextured surfaces

With the purpose of analysing the effects of different geometries on the performance and improvement of the surface and thermal characteristics at microscale, the manufacture and characterisation of the microtextured surfaces were carried out. The selection of the texture geometries was based on the authors' prior work [12, 34]. Considering the limitations of manufacturing these highly complex natural surface

Table 1 Cases tested numerically using Hydro3D for code validation

Approach	Riblet space s (mm)	Riblet height h (mm)	Riblet thickness t (mm)	Bulk velocity (m/s)	h/s ratio	Dimensionless space s^+	Dimensionless height h^+	Dimensionless thickness t^+
Varying bulk velocity	0.40	0.2	0.0125	5.0	–	10	5.0	0.30
	0.40	0.2	0.0125	3.0	–	17	8.5	0.48
	0.40	0.2	0.0125	2.0	–	23	11.5	0.65
	0.40	0.2	0.0125	1.5	–	34	17.0	0.87
	0.40	0.2	0.0125	1.0	–	50	25.0	1.15
Varying space	0.40	0.2	0.0125	–	0.5	17	8.5	0.48
	0.25	0.2	0.0125	–	0.8	23	8.5	0.48
	0.20	0.2	0.0125	–	1.0	34	8.5	0.48

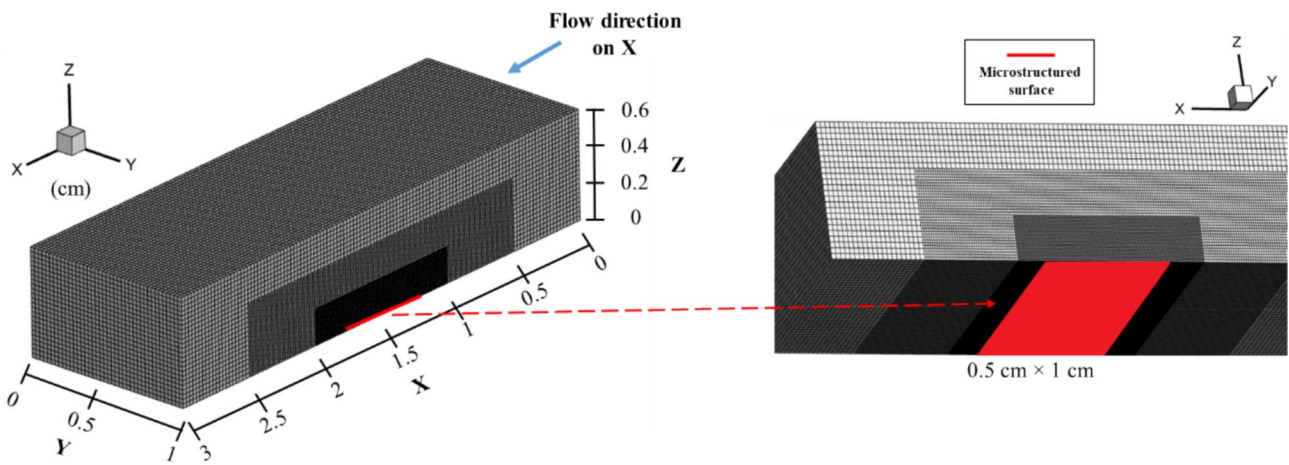
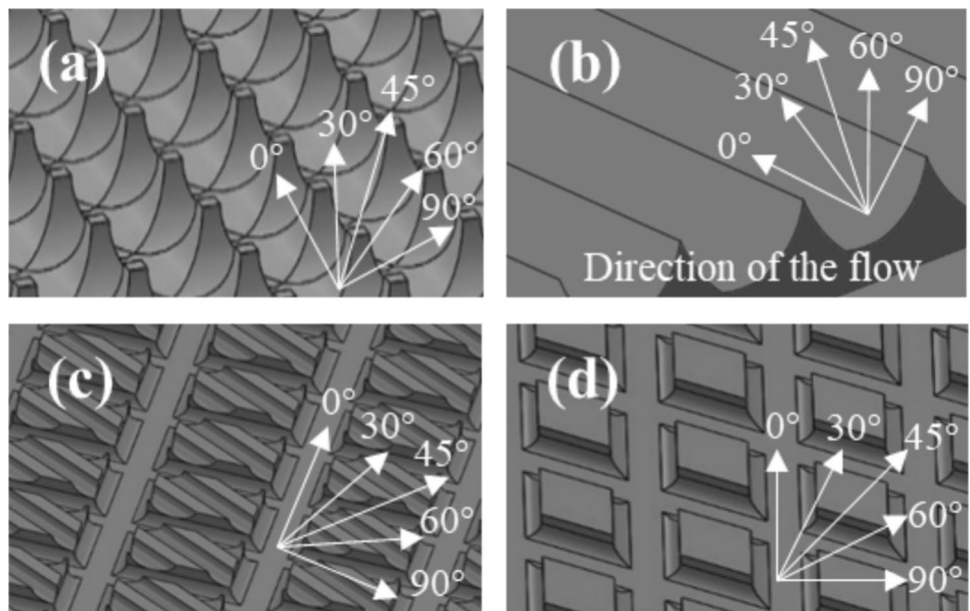


Fig. 3 Computational domain with microtextures

Fig. 4 Computer-aided design (CAD) of the microtexture geometries and the angles of action against the flow direction: **a** Lotus, **b** Scallop, **c** Sharkskin and **d** Diamond [34]



geometries, simpler designs based on the sharkskin and lotus leaves, such as diamond and scallop textures, respectively, were also generated.

3.1 Manufacturing technique

Prior to the fabrication of the microtextures, grade 316L stainless steel inserts were manufactured via casting, followed by conventional turning and facing operations with a final roughness (R_a) of 0.2 μm . The total height of the inserts was 25 mm; the top 15 mm had a diameter of 25 mm while the bottom 10 mm had a diameter of 28 mm (Fig. 5a). The selected microtexture geometries were produced on the planar top faces of the stainless steel inserts via micro-wire electrical discharge machining (μ -WEDM), using 100- μm -diameter wires. Nominal dimensions of the microtexture geometries are shown in Table 2. These designs were based on the numerical results and the restrictions associated to the smallest available micro-wire diameter (50 μm) for manufacture. Further details on the Wire-DEM manufacturing process and the optimisation of the process parameters are given in [12, 34].

3.2 Characterisation of the microtextured surfaces

The CAD drawings of each of the microtexture geometries are shown in Fig. 4. After creating the inserts, the characterisation of the final products was executed by using a 3D area scanning optical profiler (Sensofar Smart) and by high-resolution surface topography analysis via scanning electron microscopy (SEM). For the characterisation, five areas of dimension 1.7 mm \times 1.4 mm were scanned on the textured 25-mm inserts' top face, the approximate locations of which are shown in Fig. 5b. Each of the scanned areas was divided into three sections from where five measurement points were chosen as seen in Fig. 5c. Then at each point, three different

Table 2 Design specifications (nominal dimensions) for each microtexture geometry

Geometry	Width of grooves (μm)	Depth of grooves (μm)	Width of riblets (μm)
Lotus	130	65	25
Scallop	100	75	25
Sharkskin	520	130	260
Diamond	280	130	260

groove characteristics were measured: widths and depths of the grooves, and widths of the riblets [35], as depicted in Fig. 5d.

3.3 Wettability characterisation of the microtextured surfaces

Surface wettability not only depends on the droplet properties, but also on a wide range of parameters including the surface roughness or the surface microtexture. The interface, where liquid, solid and gas coexist, is called the contact line [36]. The experimental approach uses a shadowgraph configuration with a high dynamic range (HDR) mode imaging and image analysis to obtain the contact angle between the water droplets and the different microtextured surfaces.

For this study, single water droplets of 0.05 mL volume were generated by a 3.0-mL pipette and were allowed to travel vertically downwards towards the different microtextured surfaces. The distance between the pipette and the microtextured surfaces was 10 mm (Fig. 6).

The image analysis was performed using ImageJ. Two different plug-ins were used and manually corroborated using a virtual protractor. The first plug-in, 'DropSnake', is based on B-spline snakes (active contours) to shape the drop [37]; while the second plug-in, 'LBADSA' (Low-Bond

Fig. 5 **a** An untextured insert manufactured via casting followed by machining; **b** schematic diagram of the inserts' top face showing the five locations of scanned regions; **c** locations of the measurements taken within one scanned area; **d** locations of the grooves' measured characteristics

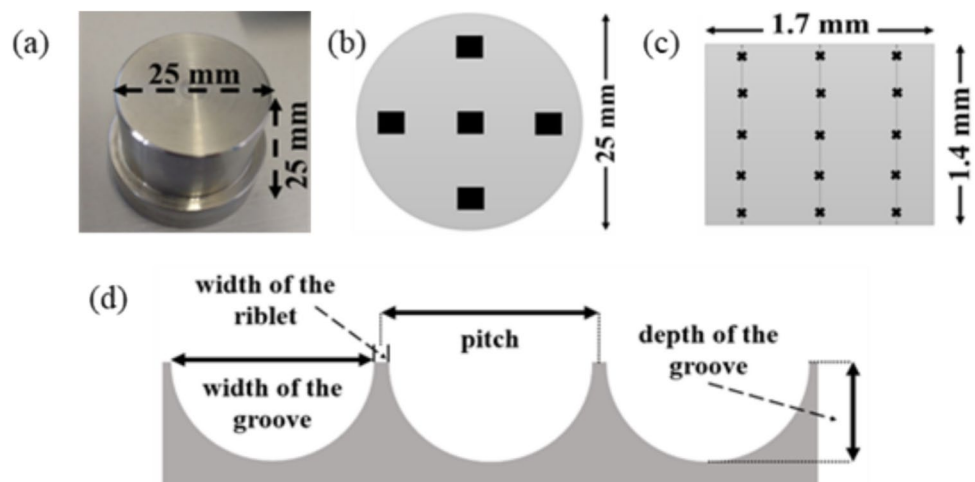
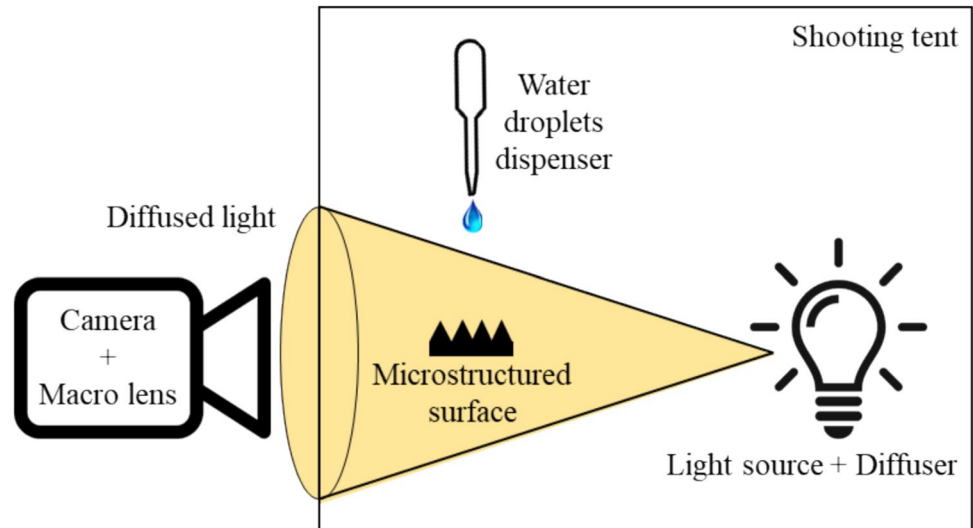


Fig. 6 Shadowgraph configuration diagram



Axisymmetric Drop Shape Analysis), is based on the fitting of the Young–Laplace equation to the image data [38]. The wettability experiments were repeated 20 times for each microtextured surface.

High contact angle surfaces are known as hydrophobic ($90\text{--}150^\circ$) or super-hydrophobic ($+150^\circ$) surfaces; they present a low degree of wetting, which indicates a low solid surface energy or chemical affinity. Conversely, surfaces with a low contact angle are known as hydrophilic ($10\text{--}90^\circ$) or super-hydrophilic ($0\text{--}10^\circ$).

4 Experimental evaluation of boundary layer and drag

The purpose of the velocity profile experiments is to evaluate the performance of the microtextured surface geometries at different angles of action, i.e. 0° , 30° , 45° , 60° and 90°

(see Fig. 4), against the airflow direction for better boundary layer control and drag reduction.

4.1 Experimental apparatus

The air duct test rig was specially designed to test the 25-mm inserts with microtextured surfaces under isothermal diffusion turbulent flow in a cost-effective way. The duct rig was composed of a centrifugal fan, two rotameters, a support disc for the inserts, a unislide and a hotwire anemometer (see Fig. 7).

The maximum delivered flow by the pipe system is 3000 L/min, the delivery pipe has two air rotameters that can measure up to 2000 L/min, together with a fan of 7.5 kW, 3-phase motor power rating. The test section contains an entry hole on the top of the duct for the stainless steel disc support. The diameter and thickness of the support disc are 76 mm and 10 mm, respectively, while a collar of 82

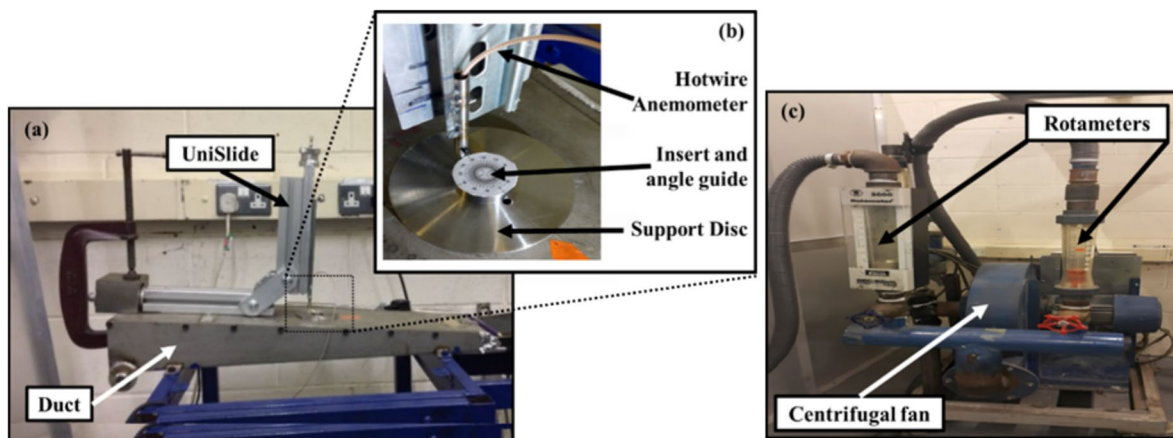


Fig. 7 Air duct test rig

mm diameter and 4 mm thickness aids in fixing the support into the hole on the duct. The support disc has a 25-mm hole for placing the microstructured insert specimens and a 4.5-mm hole for positioning the hotwire probe. The 25-mm insert has a guide of angles marked on the top together with a collar that allows it to freely rotate on the disc support (Fig. 7b). The bottom face of the 25 mm insert is ensured to be aligned with the bottom face of the support disc and the inner surface of the top part of the duct to effectively test the microstructured surface. The unislide, supplied by LG Motion, holds the hotwire probe and helps moving it precisely. The movement of the hotwire probe is 1 mm in the vertical direction for each full turn of the leadscrew. The total vertical distance that could be covered is 16 cm, with a minimum achievable distance of $10 \mu\text{m} \pm 2 \mu\text{m}$. The selection of the hotwire anemometer was based on the 'Hot-wire and Hot-film Probe Selection Guide' by Dantec Dynamics. The hotwire system used in this study consists of a 55P11 probe, MiniCTA 54 T42 and StreamWare Basic software. The 55P11 Probe is designed to measure one-dimensional velocities up to 100 m/s in air flows.

4.2 Experimental design

The experiments were conducted in the air duct test rig (shown in Fig. 7) with turbulent air flow under isothermal and atmospheric conditions using a hotwire anemometer to measure velocities in the boundary layer. Each set of experiments took 7 h and was carried out four times on different days to corroborate repeatability. Three velocity measurements were undertaken for each texture geometry, angle and position from the wall in the vertical direction to obtain the velocity profiles in the boundary layer. The duct had an internal height of 20 mm (20,000 μm) at the test area. Therefore, considering that the boundary layer thickness is defined as the distance between the wall and the point where the velocity reaches 99% of the free stream velocity and assuming that the free stream velocity is approximately located at 10 mm (10,000 μm) from the wall, velocity measurements were taken at every 100 μm from the wall until the distance reached 1000 μm . Further measurements were taken every 1000 μm until the distance reached 13,000 μm from the wall to ensure that the velocity profiles include the full boundary layer. Based on previous studies that showed damage to the hotwire probe when working at less than 125 μm from the wall [12], this study did not consider velocities at less than 100 μm from the wall to avoid damage to the experimental apparatus.

In order to provide a fully developed turbulent flow, ten experiments were performed to find the most reliable flow rate delivered by the system. Furthermore, to validate and compare results with the numerical simulations conducted

in the present study as well as with that reported in the literature [31], the Reynolds number range that was used for drag reduction experiments was between 8000 and 13,000. As a result, a flow rate of 1000 L/min was selected. The hotwire calibration system for this study was previously validated by using a Laser Doppler Anemometry (LDA) at the same conditions with 10- μm seeding particles [12]. Thus, for every experimental run, a set of velocities was measured at different flow rates (0, 250, 350, 450, 550, 650, 750, 850, 950, 1000, 1050, 1150, 1250 L/min) using an AF210 anemometer to develop a calibration curve for the hotwire anemometer system.

The outer edge of the velocity boundary is typically defined by $u = 0.99U_\infty$, thus the boundary layer thickness (δ) is defined as:

$$\delta = \delta(x) = y_{(u=0.99U_\infty)} \quad (3)$$

where U_∞ is the free stream velocity and $y_{(u=0.99U_\infty)}$ is the distance from the surface at which the velocity is equal to 99% of the U_∞ .

The drag force (D) was calculated as follows:

$$D = \rho_\infty b \int_0^{hy} u(U_\infty - u)dy = \rho_\infty b U_\infty^2 \int_0^{hy} \frac{u}{U_\infty} \left(1 - \frac{u}{U_\infty}\right) dy \quad (4)$$

where hy is the height and b width of the plate.

5 Experimental evaluation of condensation heat transfer

The objective of the condensation heat transfer experiments is to evaluate the effectiveness of the microstructured surface geometries to facilitate nucleation, growth and condensate drainage, in order to enhance heat transfer through the increase of surface temperature differential (ΔT_s). Research in this area has been successfully undertaken using different surface modification techniques to increase heat transfer and detachment of droplets while delaying surface flooding [8]. Surface condensation can take place through two mechanisms: dropwise condensation (DWC) and filmwise condensation (FWC). Numerical and experimental studies demonstrated heat transfer enhancement when grooved surfaces are used to decrease liquid film thickness. In addition, Orejon et al. [13] demonstrated notable heat transfer performance with simultaneous DWC/FWC by varying the microtextured surfaces' design parameters despite the fact that FWC offered an order of magnitude lower heat transfer coefficients than DWC due to the thickness of the liquid film covering the solid surface [11].

5.1 Experimental apparatus

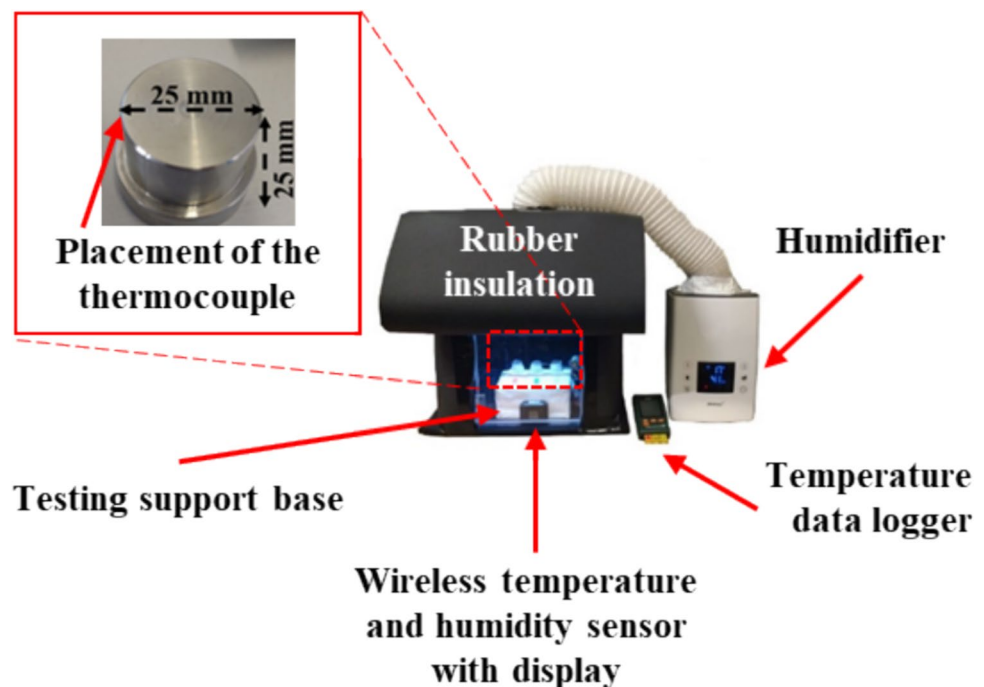
The experimental apparatus was designed to test the four microtextured inserts with respect to an untextured insert. The apparatus consists of three main parts: condensation chamber, data acquisition/control system and humidifier system (Fig. 8). The condensation chamber consisted of a 400 mm × 400 mm × 500 mm Perspex chamber with a visualisation window of 250 mm × 300 mm; a 100 mm diameter opening at the top for the entry of humid air from the humidifier; a 20 mm × 20 mm opening on the bottom sidewall to connect the inserts with the data acquisition system and another similar opening at the bottom of the back wall to drain the condensate out of the chamber. The chamber was insulated with a 13-mm-thick nitrile rubber sheet to reduce heat loss and surface condensation. There was an insulated testing support base of 180 mm × 130 mm inside the chamber for three inserts to be placed on, with a 20-mm separation space between them. Each insert had a 0.9-m-long bead wire subminiature type-K thermocouple probe attached near the microtextured surface (Fig. 7). The thermocouples were connected to a 3-Channel LCD temperature data logger, with an accuracy of $\pm(0.5\% + 0.5^\circ\text{C})$ from -100 to $+1300^\circ\text{C}$, which was part of the data acquisition/control system outside the chamber. The data acquisition/control system also consisted of a wireless temperature and humidity sensor with display inside the chamber with a temperature accuracy of $\pm 0.5^\circ\text{C}$ from 0 to $+40^\circ\text{C}$ and a humidity accuracy of $\pm 2\%$ typical from 20 to 80% and $\pm 5\%$ maximum from 0 to 100% . The displayed data was used

to control the temperature inside the chamber using a fan that blew air through nichrome wire coils before starting the humidifier to increase the humidity in the chamber. A temperature, humidity and dew point data logger with an LCD screen was used to acquire and record the conditions inside the condensation chamber with a temperature accuracy of $\pm 0.55^\circ\text{C}$ typically from 5 to 60°C and a humidity accuracy of $\pm 2.25\%$ from 20 to 80% and $\pm 3\%$ maximum from 0 to 100% at temperatures up to 60°C . Finally, the humidifier contained an ultrasonic water vaporiser, a temperature and %RH sensor and an air humidity control that delivered flows between 250 and 400 mL/h .

5.2 Experimental design

For the thermal experiments, the following arguments were taken into consideration: (1) The rate of heat transfer (\dot{Q}) is directly proportional to the surface temperature differential (ΔT_s). Hence, ΔT_s was chosen as the main parameter in this study to analyse the effects of the microtextured surface geometries during condensation. (2) The humid flow velocity entering the condensation chamber is very low (0.15 m/s), thus the interfacial shear between the liquid and the vapour is negligible [11]. (3) Taking into account the application of the microtextured surfaces in energy recovery systems where the condensation phenomenon occurs under humid environments, the temperature and relative humidity in the condensation chamber were set up to $301.57\text{ K} \pm 0.5\%$ and $96 \pm 3\% \text{RH}$ and $1.02\text{ bar} \pm 0.5\%$ according to the statistical analysis and

Fig. 8 Experimental apparatus for the condensation heat transfer experiments (adapted from [35])



collection of data by The National Oceanic and Atmospheric Administration (NOAA) [39].

The inserts were insulated with waterproof insulating tape, leaving the top surface open for testing. The thermocouples for the temperature measurement were placed inside the insulating area, right at the edge between the top and side faces. Each set of experiments was carried out for a period of 8 min under stable conditions. Temperature and %RH measurements inside the chamber were recorded every 10 s whereas the inserts' surface temperatures were measured after every 20 s. With the recorded data, two differential temperatures were calculated: the inserts' surface temperature differential (ΔT_s) which is the difference between the final temperature of the insert and its temperature at the beginning of the experiment, and the surface subcooling temperature differential (ΔT) which is defined as the temperature difference between the humid air and the surface temperature. Consequently, the specific heat absorbed by the inserts (Q) in joules, the rate of heat transfer (\dot{Q}) in watts, heat flux (q) in W/m^2 and heat transfer coefficients (h) in W/m^2K were calculated as follows:

$$Q = m \times Cp \times \Delta T_s \tag{5}$$

$$\dot{Q} = Q \times t \tag{6}$$

$$q = \dot{Q}/A_s \tag{7}$$

$$h = q/\Delta T \tag{8}$$

where m is the mass of the insert in kg, Cp is the specific heat capacity of the 316L stainless steel in J/kgK , t is time of the experiment in seconds, and A_s is the surface area in m^2 .

6 Results and discussion

6.1 Manufacture and characterisation of the microtextured surfaces

The microtextures' characterisation results, obtained from the 3D optical profilometer, together with the percentage deviations from the nominal dimensions, are shown in Table 3. The 3D-scanned surfaces, in addition to scanning electron microscope (SEM) images, are presented in Fig. 9 against the corresponding computer-aided designed (CAD) geometries. It is observed that widths of the grooves are more closely achievable with respect to the nominal dimensions, compared to the depths of the grooves and the widths of the riblets (unmachined regions in between the machined grooves). This is because the movement and tool wear of the wire can be more precisely controlled during wire-EDM, than the occurrence of the thermo-electric interaction between the wire and the workpieces. Further, the real-life bio-inspired structures (Lotus and Sharkskin) were more challenging to imitate due to the inherent manufacturing process limitations. In contrast, the simplified textures (Scallop and Diamond) were relatively easier to generate. Thus, the deviations from the nominal dimensions were also considerably lower (-0.58 to -6.38%) for the latter two designs.

The microtextured surfaces' wettability characterisation results (contact angles), together with the standard errors, are presented in Table 4. Additionally, images of the contact angles between the water droplets and the different micro-geometries are shown in Fig. 10. While the untextured surface's contact angle was $81.41^\circ \pm 2.66^\circ$ and was considered generally hydrophilic, the Scallop texture showed

Table 3 Characterisation data for the microtextured surfaces and percentage difference with respect to the nominal dimensions

Geometry	Parameters	Width of grooves	Depth of grooves	Width of riblets	Surface area with texture (m^2)	Surface area without texture (m^2)
Untextured		–	–	–	–	0.00049
Lotus	Nominal dimension (μm)	130	65	25	0.00058	
	Measured dimension (μm)	126.21	54.79	16.66		
	Percentage difference (%)	- 2.92	- 15.71	- 33.36		
Scallop	Nominal dimension (μm)	100	75	25	0.00107	
	Measured dimension (μm)	101.56	75.63	26.53		
	Percentage difference (%)	+ 1.56	+ 0.84	+ 6.12		
Sharkskin	Nominal dimension (μm)	520	130	260	0.00057	
	Measured dimension (μm)	448.08	71.22	323.71		
	Percentage difference (%)	- 13.83	- 45.22	+ 24.50		
Diamond	Nominal dimension (μm)	280	130	260	0.00070	
	Measured dimension (μm)	278.39	121.71	251.70		
	Percentage difference (%)	- 0.58	- 6.38	- 3.19		

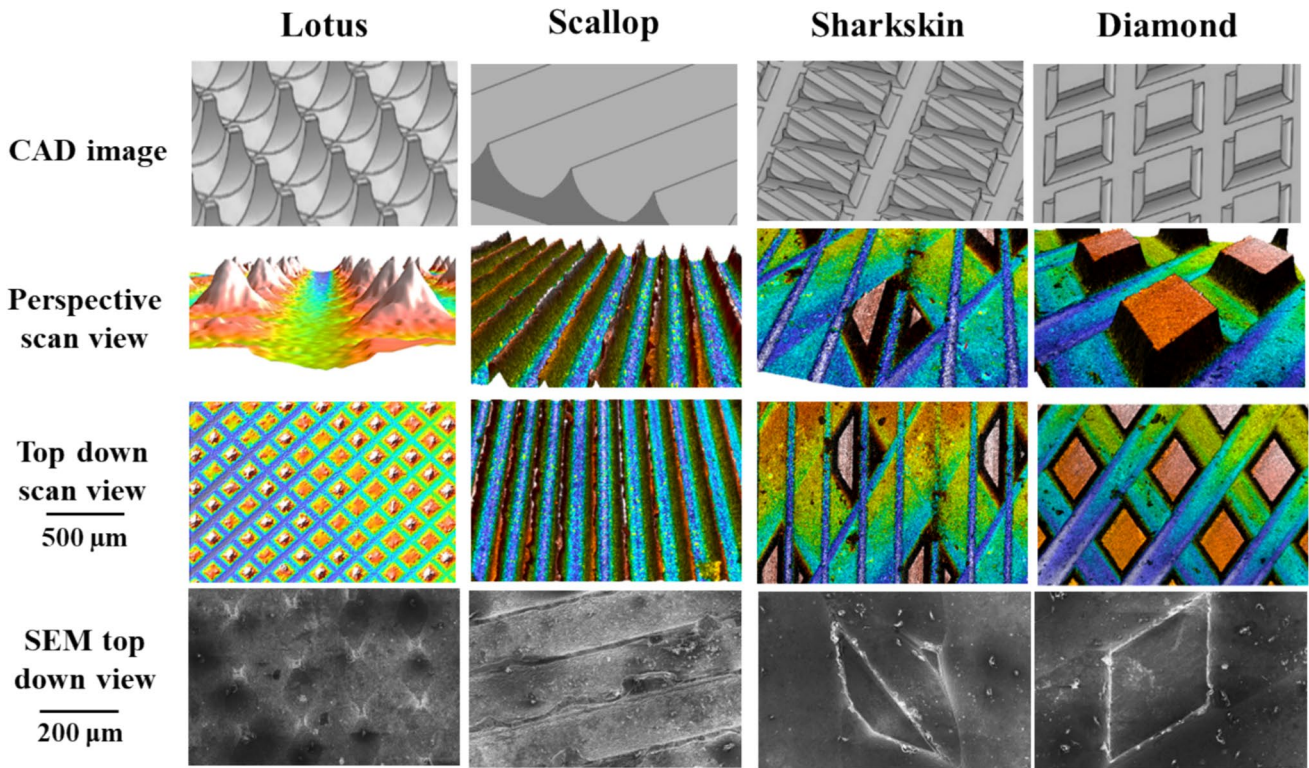


Fig. 9 CAD designs and scanned microtextured surfaces using a 3D optical profilometer (Sensofar), together with their corresponding SEM micrographs [34, 35]

Table 4 Wettability characterisation data for the microtextured surfaces, together with the standard errors

Micro-geometries	Contact angle (°)	Standard error	Wetting state
Untextured surface	81.41	2.66	Hydrophilic
Lotus	117.60	4.61	Hydrophobic
Scallop	56.20	2.65	Hydrophilic
Sharkskin	90.80	2.77	Hydrophobic
Diamond	131.47	2.92	Hydrophobic

lesser hydrophilic properties, with the contact angle varying around $117.6^\circ \pm 4.61^\circ$. The Diamond geometry exhibited close to superhydrophobic characteristics, with a contact angle of $131.47^\circ \pm 2.92^\circ$. It is also noted that designs that contained grooves along one direction (Scallop and Sharkskin, from Fig. 9) typically showed lower contact angles, because the water droplets spread along the channels. Conversely, cross-hatch patterns (Lotus and Diamond) exhibited greater contact angles.



Fig. 10 Contact angles between water droplets and the textured and untextured surfaces

6.2 Numerical analysis

In order to validate the Hydro3D code, the dimensions of the geometries studied in [24, 32, 33] were used in the code input file, and the drag reduction results were grouped in two sets of $s+$ values, with an angle of action of 0° (Fig. 11). The first set of data was obtained by varying the velocity while the second set was recorded by varying the space between the riblets (Table 1). The first set of results (Fig. 11a) presented good agreement with the literature, showing that, for the range of $s+$ between 0 and 45, the drag reduction followed the same tendency before diverging with high $s+$ (> 45). The results of the second set (Fig. 11b) also present fair alignment with the literature by exhibiting similar trends within a range of $s+$ between 0 and 30, before starting to diverge from the findings of [24, 32, 33]. In both approaches, the drag reduction increases after $s+ = 20$ due to eddies forming between the riblets and creating interference between the flow and the surface that reduces the friction and drag consequently.

For the numerical analysis, the velocity gradient at the wall (du/dz) is presented in Fig. 12 for an untextured surface, as well as for the riblet base and tip of a microtextured surface. For the microtextured surface, it is found that the velocity gradient increases with sharp fluctuation when moving up from the base towards the riblet tip due to the presence of the riblets. However, the results show that the untextured surface exhibits a higher velocity gradient (up to 142 s^{-1}) than the riblet tip (up to 94 s^{-1}) and the riblet base (up to 23 s^{-1}).

In terms of drag reduction, the shear stress at the wall plays a significant role in the transition from laminar to turbulent conditions and its integration with the area is directly

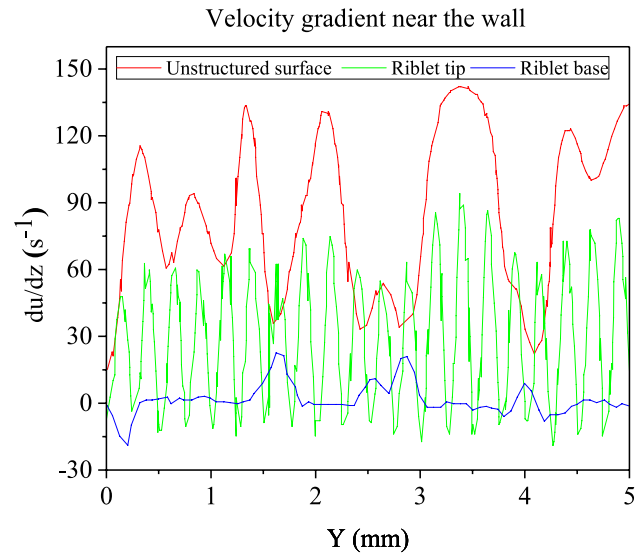


Fig. 12 Velocity gradient near the wall of an unstructured/untextured surface, as well as near the riblet base and riblet tip of a microtextured surface (blade geometry)

proportional to the drag force [40]. The wall shear stress is a function of the viscosity and the velocity gradient at the wall. The effect of microtextures on the shear stress near the wall against an untextured surface is shown in Fig. 13. The shear stress in the microtextured surface is between 44.5 and 89% which is less than that generated in the untextured surface. This is because the riblets maintain the vorticities over the riblet tips, leading to the reduction of velocity fluctuation near the wall and thus decrease the surface area attached to the high-velocity fluctuations, which in turn reduces the wall shear stress.

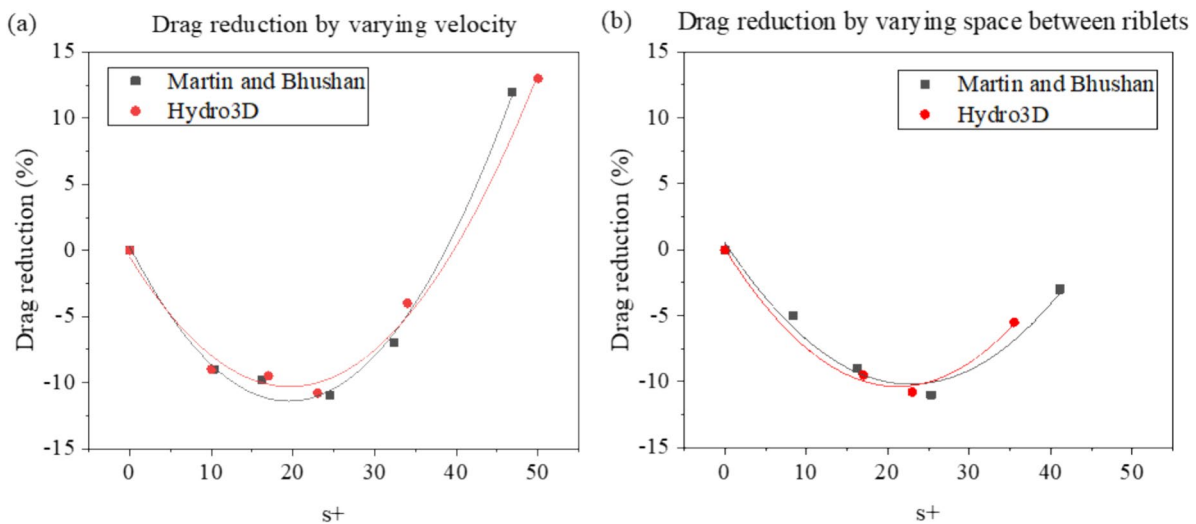
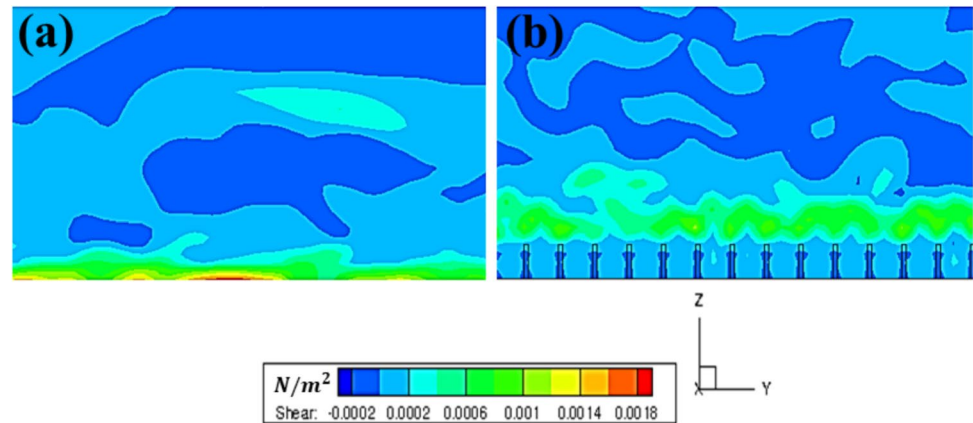


Fig. 11 Validation of the code through drag reduction as a function of $s+$. **a** Approach 1: Varying velocity with $h/s = 0.5$. **b** Approach 2: Varying space between riblets with constant height h

Fig. 13 Shear stress (N/m^2) near the wall for **a** untextured surface and **b** microtextured surface (blade geometry of height = $200\ \mu m$ and width = $280\ \mu m$)



Following the same procedure and under the same conditions, the numerical results of the velocity distribution and shear stresses on the selected microtexture geometries are shown in Figs. 14 and 15 and Table 5.

Figure 14 shows the axial velocity distribution (U/Um) in the channel, where U is the local velocity in the X-direction and Um is the bulk velocity at the inlet. The results show the effects of viscosity on the laminar sublayer and how the momentum transfer from the turbulent layer counteracts the wall effects on the buffer zone. The boundary layer thickness can be found at $U/Um = 0.99$. After this point, the effect of the wall completely disappears, and the flow velocity attains the mainstream velocity value or the bulk velocity. With higher velocities Reynold Numbers increase, thus the momentum near the wall considerably increases, allowing the boundary layer to withstand a larger unfavourable pressure or positive pressure gradient [41]. This positive pressure results in higher wall shear stress (Fig. 15) and drag (Table 5).

6.3 Experimental evaluation for drag reduction and boundary layer control

In relation to the effects of the microtextured surfaces on drag reduction, numerical simulation results show higher drag reduction (by 6.1–6.7%) in comparison to the untextured surface. The experimental results also exhibit similar trends of drag reduction when using the textured surfaces; however, the experimental average drag reduction (10.75%) was almost twice the values predicted by the numerical models (4.98% average value) when compared against an untextured surface. This experimental result is comparable to the 9.9% drag reduction obtained by Bechert et al. [42]. The difference between drag reduction values predicted and experimentally measured was possibly because of some unmodeled factors, such as the viscosity of the real surfaces and the turbulence in the air flow. Figure 16a shows the effects of the microtexture geometry and the angle of

action on drag reduction. The geometry with the highest drag reduction effect in comparison to an untextured surface was Lotus (16.9%), followed by Scallop (9.8%), Diamond (9.4%) and finally Sharkskin (6.9%), with standard errors of the mean of 0.12, 1.67, 0.96 and 0.99, respectively. In each of the geometries, the maximum drag reduction was observed at the 0° angle of action. However, the angle of action's effect had a minor impact on the drag reduction when compared to the geometry's contribution. For Lotus, there was a difference of 1% only between the angles of action associated with the highest and lowest drag reduction. For the Scallop structure, this difference was 2.9%, while that for the Sharkskin and Diamond geometries were 2.5% and 1.6%, respectively.

One interesting finding was the reduction of the boundary layer thickness (δ) in Fig. 16b. The Lotus geometry with a 0° angle of action (θ) exhibited the highest δ reduction (12.6%), followed by Scallop with $\theta = 45^\circ$ (9.1%), Diamond at $\theta = 45^\circ$ (7.8%) and Sharkskin at $\theta = 0^\circ$ (5.7%), with standard errors of mean of 0.38, 1.54, 1.94 and 0.87, respectively. The differences between the highest and lowest δ reduction with respect to the angles of action for each geometry were as follows: 3% for Lotus, 1% for Scallop, 0.5% for Diamond and 1% for Sharkskin structure.

6.4 Condensation heat transfer experiments

Figure 17 presents the results of the condensation experiments after 8 min in the condensation chamber. The surface temperature differentials (ΔT_s) in the Lotus, Scallop, Sharkskin and Diamond textured surfaces were higher by 8.57%, 22.86%, 17.14% and 25.71%, respectively, than the untextured surface.

The highest ΔT_s was observed with the Diamond geometry. Previous work by Chatterjee et al. [43] also reported a 25% improvement in the heat transfer while Qi et al. [11] found that grooved surfaces can enhance heat transfer by 50% when compared with smooth surfaces. Additionally,

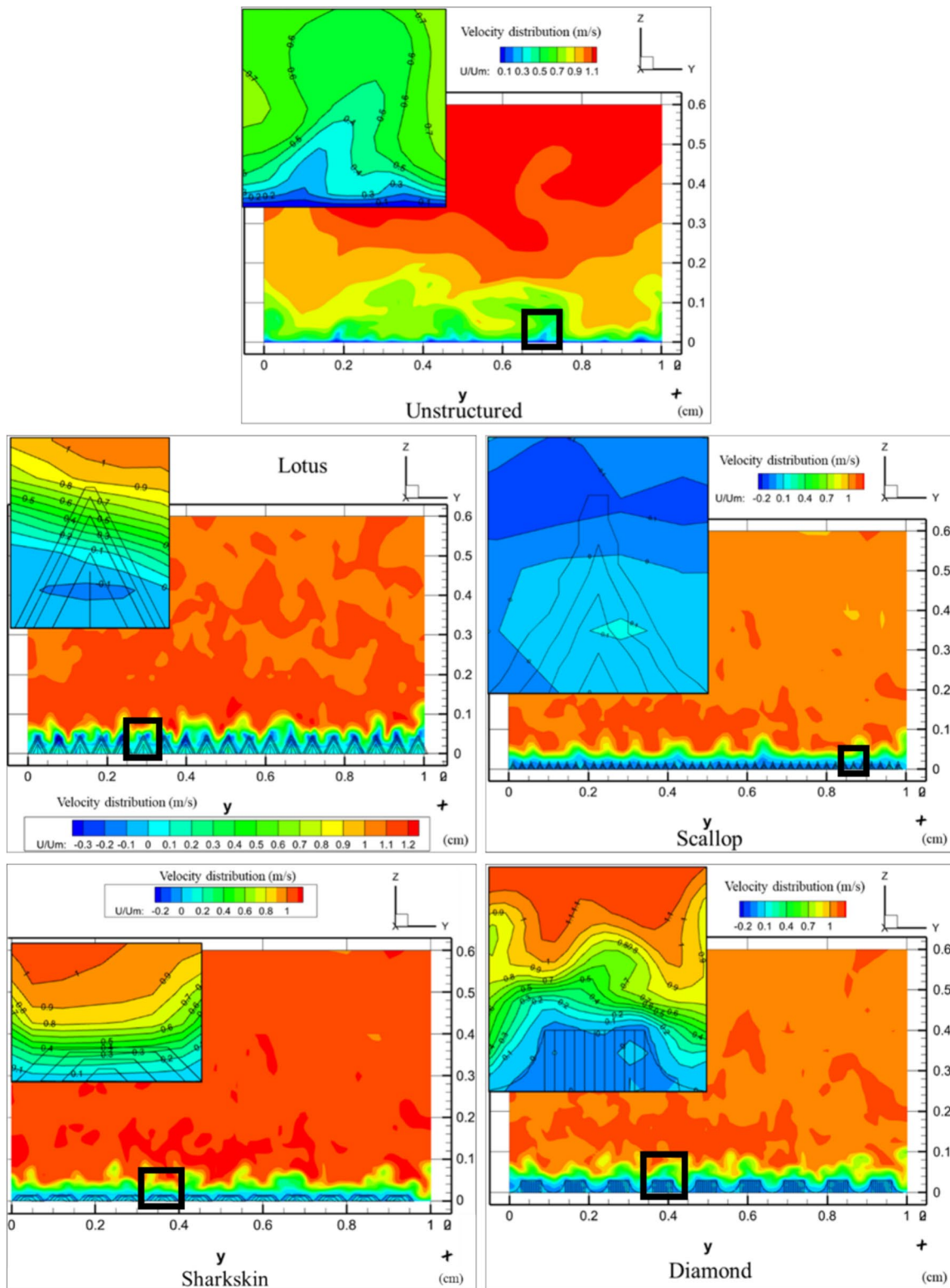


Fig. 14 Velocity distribution (m/s) near the walls of the untextured and textured specimens (inset images show the magnified areas)

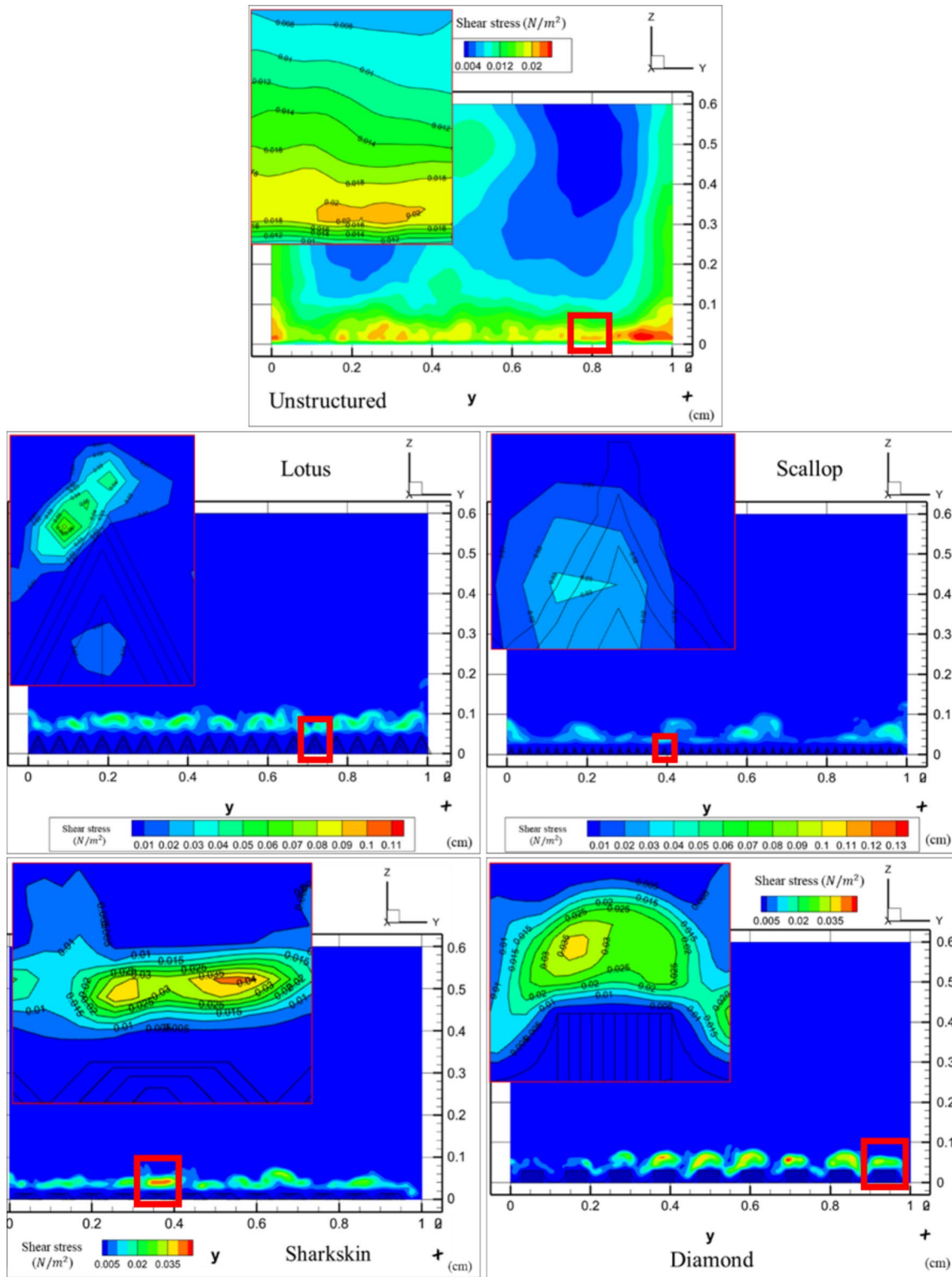


Fig. 15 Shear stresses (N/m^2) near the walls of the untextured and textured specimens (inset images show the magnified areas)

when considering the larger superficial area (A_s) that the microtextures represent, the specific heat (Q), heat rate (\dot{Q}) and heat flux (q) are 6.6–36% greater than that of the

untextured insert, while the heat transfer coefficient (h) is between 6.36 and 20.83%. The wettability property of the textured surfaces appears to have effects on the extent of

Table 5 Numerical results of the different micro-geometries

Micro-geometries	Untextured	Lotus	Scallop	Sharkskin	Diamond
Drag reduction (%)	-	6.6	6.7	0.5	6.1
Pressure gradient (Pa/m)	0.8	13.5	14.7	1.5	14
Riblet space, s (μm)	-	250	110	520	320
Riblet height, h (μm)	-	135	80	230	155
Dimensionless space, $s +$	-	16	17	17	18

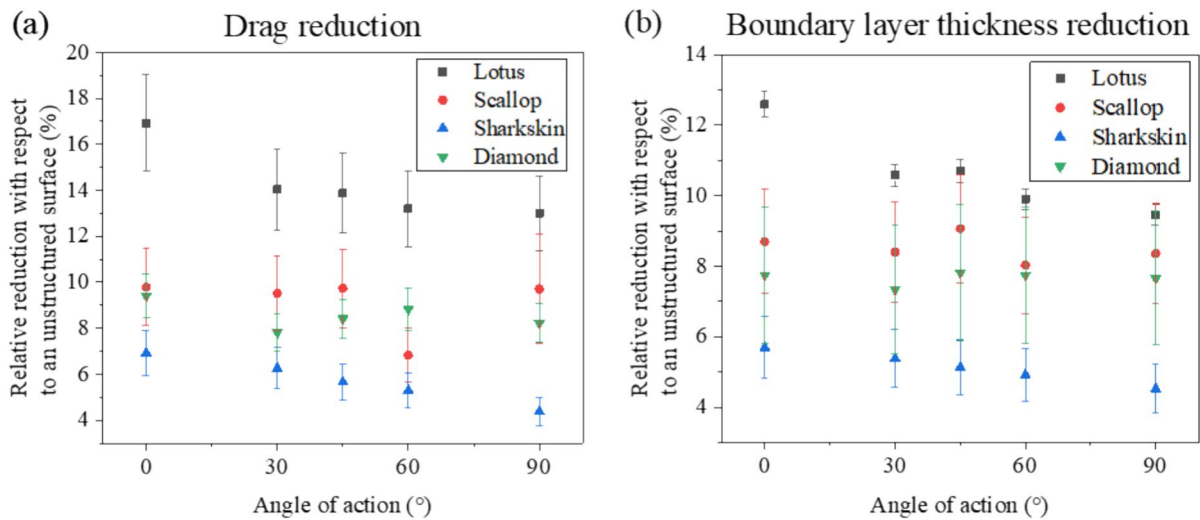


Fig. 16 a Experimental drag reduction, b experimental boundary layer thickness reduction

heat transfer. Greater hydrophilicity (Scallop texture) or hydrophobicity (Diamond texture) is thought to be linked with the higher differential temperatures obtained with these micro-geometries.

Figure 18 displays the condensation heat transfer performance based on heat flux (q) and heat transfer coefficient (h) as a function of the surface subcooling temperature differential (ΔT). The results are comparable with the work carried out by Wen et al. [44]. The obtained coefficients (in the range of 150 to 800 W/m²K) follow a similar trend reported by Ghosh et al. [45] and Mahapatra et al. [46] in which condensation heat transfer coefficients were in the ranges of 30–90 W/m²K and 30–120 W/m²K, on patterned aluminium surfaces with chemical coatings. This infers that microtextured surfaces without chemical coating can promote higher heat transfer coefficients than untextured and chemically treated surfaces.

Visualisation of the condensation after 8 min, shown in Fig. 19, displays an active dropwise condensation (DWC) on the microtextured surfaces and an inversely proportional relationship between the droplet size and the ΔT_s . This observation is in agreement with the results reported by Chatterjee et al. [43] and Wen et al. [44] in which a higher temperature differential presented a lower droplet density and size. Furthermore, three stages of a droplet life were

observed in this study: nucleation, growth, and departure. The droplets on the untextured surface reached up to the first stage after 8 min of condensation, while those on the Lotus and Sharkskin textured surfaces signalled the second stage whereas the droplets on the Diamond and Scallop surfaces were already in the final stage of their life (Fig. 19).

Although the droplets on the untextured surface were evenly distributed, the droplet life cycle was longer on this insert compared to the other textured surfaces. From Fig. 20, only three droplet life cycles are observed on the untextured surface and the Lotus structure. In contrast, the Scallop texture exhibits five, while the Sharkskin and the Diamond textured surfaces display six droplet life cycles, approximately. According to Anand et al. [47], the removal of the condensates from the surface results in a considerable increase in heat transfer. Grooten and Geld [48] also detailed that higher frequency of droplet removal reduces the probability of droplets sticking onto the condensation surface. These could in part explain the higher ΔT_s observed for the microtextured surfaces in the present study. While comparing among the various microtextures, the Diamond and Scallop structures exhibit the highest ΔT_s (Table 6), possibly due to the geometry configuration that places them closest to the superhydrophobic and superhydrophilic wetting states with respect to the other textures (Tables 4

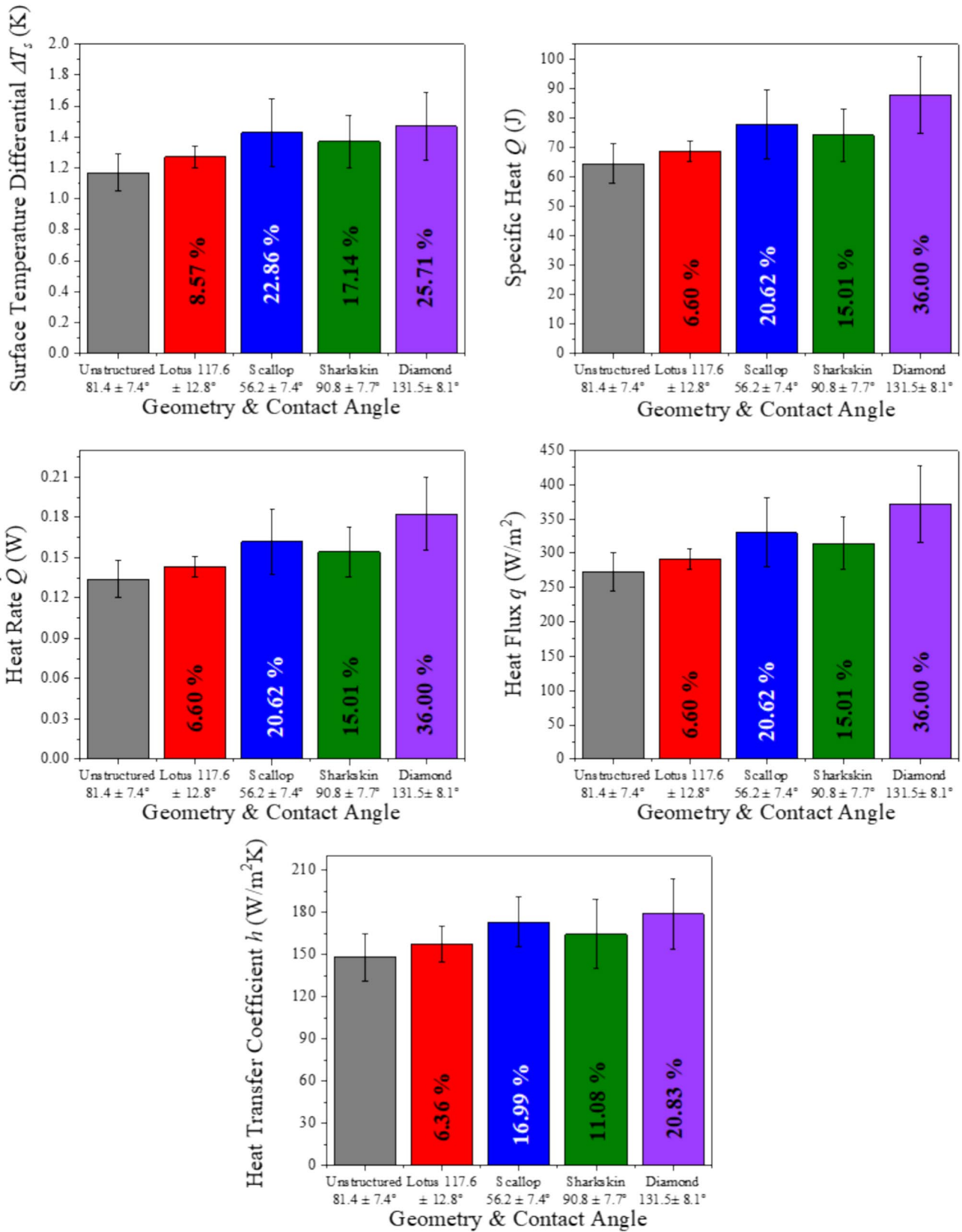


Fig. 17 Surface temperature differential (ΔT_s), specific heat absorbed by the insert (Q), heat rate (\dot{Q}), heat flux (q), and heat transfer coefficient (h) results with percentage of improvement with respect to an untextured surface

Fig. 18 Condensation heat transfer performance of textured and untextured surfaces. Heat flux (q) and heat transfer coefficient (h) as a function of the surface subcooling temperature differential (ΔT)

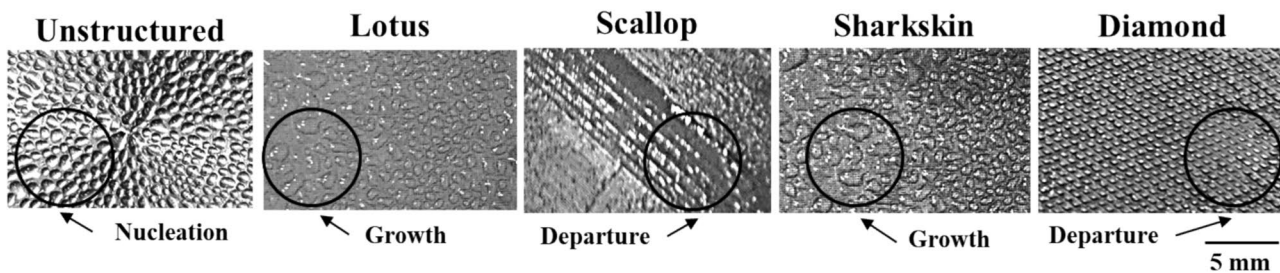
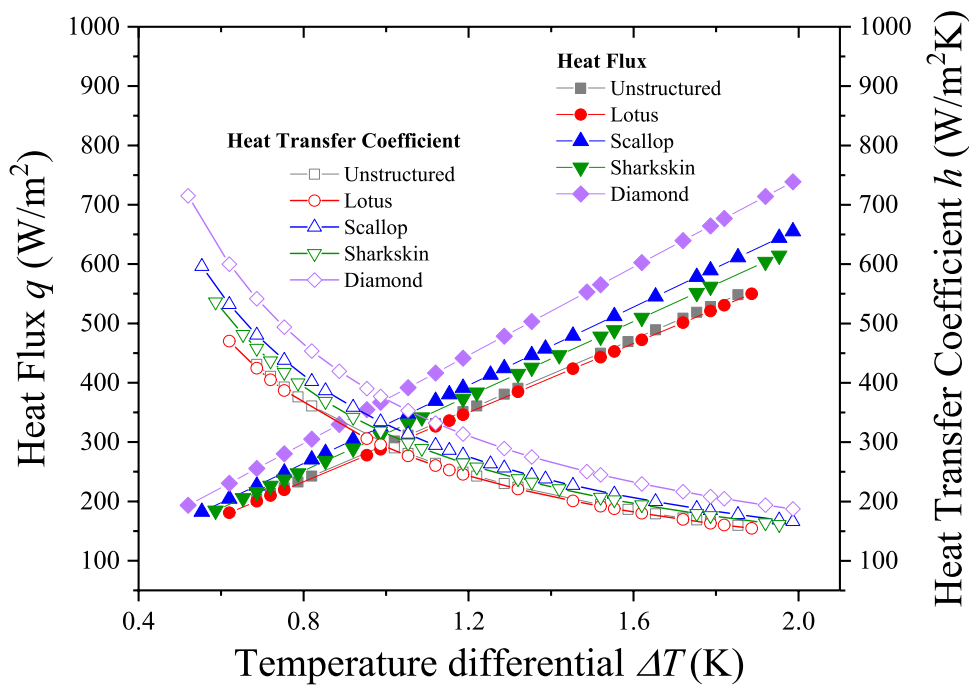


Fig. 19 Formation of condensates on the unstructured and microstructured surfaces

and 5), thereby rendering a higher condensation rate as well as a greater drainage rate. Additionally, by analysing the changes in the surface temperature trends, higher temperature change is observed at the nucleation stage whereas more stable temperature change is noted during growth. The durations of the droplet life cycles are approximately 80 to 150 s (Fig. 20). Chatterjee et al. [43] reported droplet life cycles between 9 and 12 s by visualising the condensates on copper patterned surfaces at different flows using a digital camera, whereas He et al. [49] reported cycles between 421.1 and 487.4 s for aluminium micro-/nanosurfaces with chemical coating by using optical microscopy visualisation. Further research is planned to investigate droplet life cycles to optimise the performance at each stage that can corroborate the trend of the change in temperature in order to quantify the droplet life cycles.

7 Conclusions

The present research explores the opportunities of enhancing the surface and thermal characteristics of metallic surfaces using bio-inspired microtextured geometries for applications in the energy sector. In relation to the isothermal characteristics to control boundary layer and to reduce drag, the in-house code, Hydro3D, was successfully implemented to solve the Navier–Stokes equations when turbulent flow is simulated over microtextured surfaces. The numerical and experimental results based on the microtexture geometry parameters showed similar trends for drag reduction, even though the experimental data exhibited twice the values achieved during the simulations. The Lotus and Scallop geometries rendered the best performance in terms of the isothermal characteristics enhancement, exhibiting ~17% and ~10% drag

Fig. 20 Surface temperature differential (ΔT_s) vs. time, showing droplet life cycles

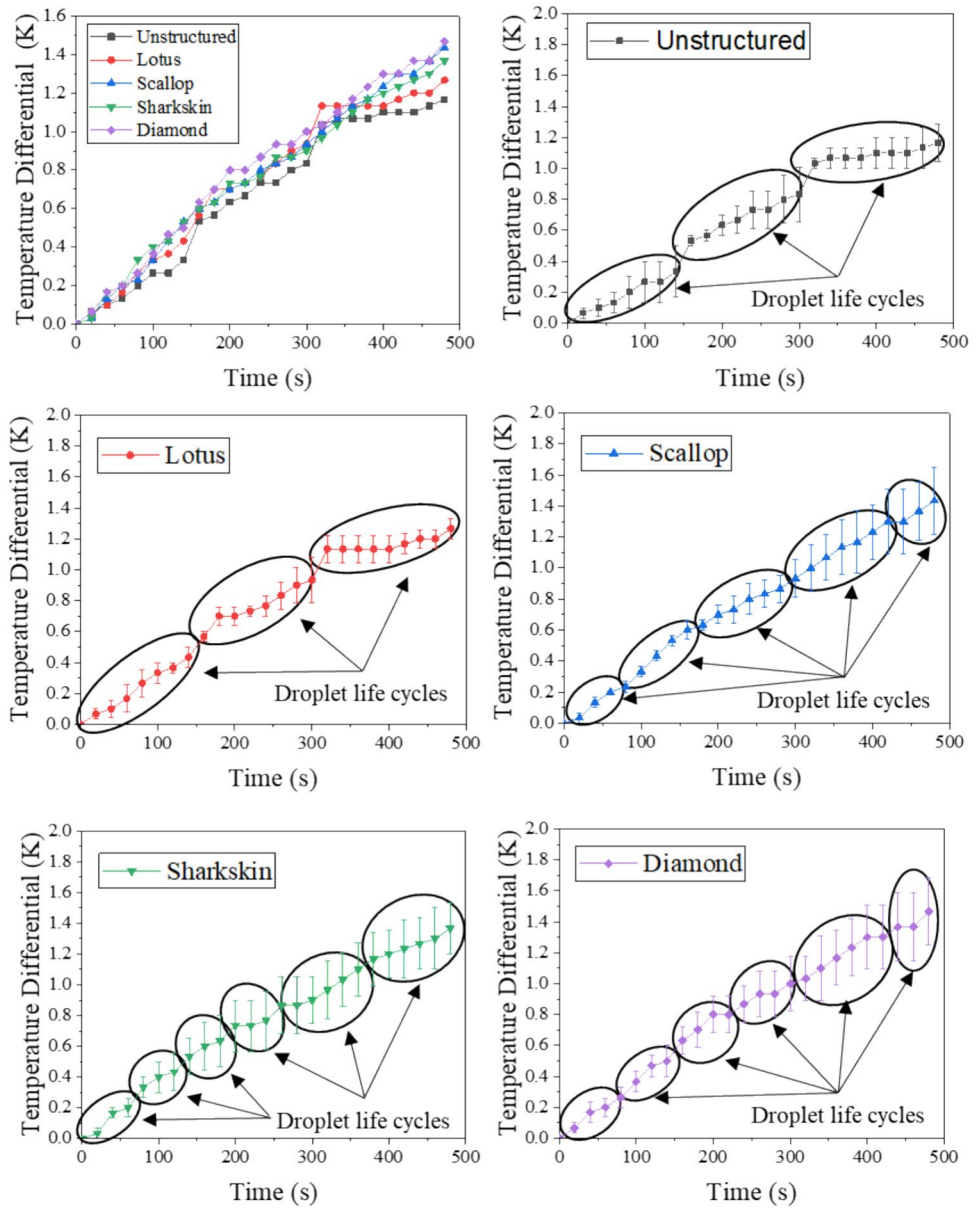


Table 6 Summary of the results from the numerical and experimental studies

Micro-geometry	Untextured	Lotus	Scallop	Sharkskin	Diamond
Numerical drag reduction (%)	–	6.6	6.7	0.5	6.1
Experimental drag reduction (%)	–	16.9	9.8	6.9	9.4
Experimental boundary layer reduction (%)	–	12.6	9.1	5.7	7.8
Contact angle (°)	81.4 ± 7.4°	117.6 ± 12.8°	56.2 ± 7.4°	90.8 ± 7.7°	131.5 ± 8.1°
Optimal angle of action (°)	-	0	45	0	45
Surface area without texture (m ²)	0.00049				
Surface temperature differential ΔT_s enhancement (%)	–	8.57	22.86	17.14	25.71
Specific heat Q and heat rate \dot{Q} and heat flux q enhancement (%)	–	6.60	20.62	15.01	36.00
Heat transfer coefficient h enhancement (%)	–	6.36	16.99	11.08	20.83
Numbers of droplet life cycles	3	3	5	6	6

reduction and ~13% and ~9% boundary layer reduction, respectively. This was due to their well-defined tips that decreased the velocity fluctuations interacting with the surface, thereby providing lower wall shear stress. Meanwhile, the angle of action against the air flow direction showed marginal effects during the study.

Regarding the thermal experiments, the results demonstrated that the condensation heat transfer performance was higher for all the microtextured surfaces. Especially, the Diamond and Scallop geometries exhibited surface temperature differentials ΔT_s 1.26 and 1.23 times higher, and other thermal parameters 1.7 and 1.36 times higher, compared to the untextured counterpart. This could be possibly attributed to the wetting properties of the Diamond and Scallop geometries, which were more hydrophobic and hydrophilic in nature, respectively, than the untextured surface tested in this study. The greater roughness of the textured surfaces could also have been attributed to the higher heat transfer capability of these specimens. Furthermore, the arrangement and size of the droplets and droplet life cycles were considerably influenced by the design of the microtexture geometries. For the Scallop pattern, this can be explained by the hydrophilic effect in which the droplets increased their size to the point of departure that facilitated condensate drainage. In contrast, the hydrophobicity of the Diamond, Lotus and Sharkskin patterns provided better droplet nucleation due to the promotion of dropwise condensation, albeit subsequent decline during the growth stage.

The simpler version of the Lotus structure, i.e. the Scallop structure, exhibited superior performance with respect to the plain surface, in terms of ~10% greater drag and ~9% higher boundary layer reduction as well as a ~23% increase in the surface temperature differential. This pattern is also easier to manufacture on different object surfaces compared to the other geometries and thus can be adopted for wider applications in the energy sector.

Finally, this research contributes to the scientific understanding of drag reduction, condensation phenomenon and droplet life cycle on microtextured surfaces that could be generated on swirl burners and heat exchangers. Future work will evaluate the possibility of implementing other manufacturing techniques, such as laser microprocessing, to create bio-inspired textured surfaces for improved heat transfer and drag reduction performance for energy and combustion system applications.

Acknowledgements All simulations are performed using the computational facilities of the Advanced Research Computing at Cardiff (ARCCA) Division, Cardiff University. Special thanks are due to Mr Anuraag Saxena (CEng and MCIBSE) for his role in the construction of the thermal experimental apparatus.

Author contribution Haydee Martinez-Zavala—main researcher, experimental work, writing—original draft.

Debajyoti Bhaduri—co-supervisor, experimental work on surface characterisation, writing—reviewing, writing and editing.

Mohamed Al-Fahham—numerical simulation work.

AgustinValera-Medina—main supervisor, conceptualisation, reviewing.

Samuel Bigot—co-supervisor, conceptualisation, writing—reviewing and editing.

Funding The research is supported by The Mexican National Council on Science and Technology (CONACYT) and The Secretariat of Energy in Mexico (SENER) [Grant Number 327757/460766] as part of the PhD project ‘High Peak, Perishable Energy Recovery—Foundation Phase’. The numerical simulation work is sponsored by the Iraqi Ministry of Higher Education and Scientific Research as part of the PhD project ‘A Modelling and Experimental Study to Reduce Boundary Layer Flashback with Microstructure’.

Declarations

Competing interests The authors declare no competing interests.

Open Access This article is licensed under a Creative Commons Attribution 4.0 International License, which permits use, sharing, adaptation, distribution and reproduction in any medium or format, as long as you give appropriate credit to the original author(s) and the source, provide a link to the Creative Commons licence, and indicate if changes were made. The images or other third party material in this article are included in the article’s Creative Commons licence, unless indicated otherwise in a credit line to the material. If material is not included in the article’s Creative Commons licence and your intended use is not permitted by statutory regulation or exceeds the permitted use, you will need to obtain permission directly from the copyright holder. To view a copy of this licence, visit <http://creativecommons.org/licenses/by/4.0/>.

References

- Kovacı H, Kavasoglu YS, Çelik A (2025) 3D printing of biomimetic hierarchical surface textures using L-PBF for improving tribological performance of Ti6Al4V alloy. *Appl Mater Today* 42:102526
- Guo C, Wu Y, Han Y, LingHu K (2023) Experimental study on influence of sharkskin denticles structure on the hydrodynamic performance of airfoil. *Ocean Eng* 271:113756
- Attinger D, Frankiewicz C, Betz AR, Schutzius TM, Ganguly R, Das A, Kim C-J, Megaridis CM (2014) Surface engineering for phase change heat transfer: a review. *MRS Energy Sustainability: A Rev J* 1:1–40
- Edalatpour M, Liu L, Jacobi AM, Eid KF, Sommers AD (2018) Managing water on heat transfer surfaces: a critical review of techniques to modify surface wettability for applications with condensation or evaporation of heat. *Appl Energy* 222:967–992
- Orazi L, Pelaccia R, Mishchenko O, Reggiani B, Pogorielov M (2020) Fast LIPSS based texturing process of dental implants with complex geometries. *CIRP Ann Manuf Technol* 69:233–236
- Tran NG, Chun D-M (2020) Simple and fast surface modification of nanosecond-pulse laser-textured stainless steel for robust superhydrophobic surfaces. *CIRP Ann Manuf Technol* 69:525–528
- Fernandez-Lucio P, Villaron-Orsorio I, Pereira Neto O, Ukar E, Lopez de Lacalle LN, Gil del Val A (2021) Effects of laser-textured on rake face in turning PCD tools for Ti6Al4V. *J Mater Res Technol* 15:177–188
- Omidvarnia F, Sarhadi A (2024) Nature-inspired designs in wind energy: a review. *Biomimetics* 9:90

9. Yu B, Xu Z, Li Z, Wang J (2025) Numerical study on heat and mass transfer of droplet collision on superheated bio-inspired surfaces. *Int J Therm Sci* 208:109476
10. Zhang C, Wang L, Crick CR, Lu Y (2025) Intelligent manipulation of liquids through the bio-inspired structuring of materials. *Progress Mater Sci* 147:101358
11. Qi B, Wei J, Li X (2017) Enhancement of condensation heat transfer on grooved surfaces: numerical analysis and experimental study. *Appl Surf Sci* 115:1287–1297
12. Al-fahham MAH (2017) A modelling and experimental study to reduce boundary layer flashback with microstructure. PhD Thesis, Cardiff University.
13. Orejon D, Shardt O, Gunda NSK, Ikuta T, Takahashi K, Takata Y, Mitra SK (2017) Simultaneous dropwise and filmwise condensation on hydrophilic microstructured surfaces. *Int J Heat Mass Transf* 114:187–197
14. Motoki S (2016) Specific microspheres increase heat transfer whilst reducing pressure losses and drag. 11th European Fluid Mechanics Conference EFMC11, Seville, Spain.
15. Rakshith BL, Asirvatham LG, Angeline AA, Raj JPS, Bose JRB, Wongwises S (2024) Experimental investigation on the heat transfer performance of flat heat pipe embedded with internally cooled condenser. *Int J Heat Mass Transf* 203:125728
16. Bechert DW, Bartenwerfer M (1989) The viscous-flow on surfaces with longitudinal ribs. *J Fluid Mech* 206:105–129
17. Chu DC, Karniadakis GEM (1993) A direct numerical-simulation of laminar and turbulent-flow over riblet-mounted surfaces. *J Fluid Mech* 250:1–42
18. Haecheon C (1993) Direct numerical simulation of turbulent flow over riblets. *J Fluid Mech* 255:503–539
19. Goldstein D (1995) Direct numerical-simulation of turbulent-flow over a modeled riblet covered surface. *J Fluid Mech* 302:333–376
20. El-Samni OA, Shun HH, Yoon HS (2005) Turbulent flow over thin rectangular riblets. *J Mech Sci Technol* 19:1801–1810
21. Zhang D, Luo Y, Li X, Chen H (2011) Numerical simulation and experimental study of drag-reducing surface of a real shark skin. *J Hydrodyn* 23:204–211
22. Jin Y, Herwig H (2014) Turbulent flow and heat transfer in channels with shark skin surfaces: entropy generation and its physical significance. *Int J Heat Mass Transf* 70:10–22
23. Benhalilou M, Kasagi N (1999) Numerical prediction of heat and momentum transfer over micro-grooved surface with a nonlinear $k-\epsilon$ model. *Int J Heat Mass Transf* 42:2525–2541
24. Martin S, Bhushan B (2016) Fluid flow analysis of continuous and segmented riblet structures. *RSC Adv* 6:10962–10978
25. Stoesser T, Nikora VI (2008) Flow structure over square bars at intermediate submergence: Large Eddy Simulation study of bar spacing effect. *Acta Geophys* 56:876–893
26. Ouro P (2017) Large-Eddy Simulation of tidal turbines. PhD Thesis, Cardiff University.
27. Fraga B, Stoesser T (2016) Influence of bubble size, diffuser width, and flow rate on the integral behavior of bubble plumes. *J Geophys Res Ocean* 121:3887–3904
28. Cevheri M, McSherry R, Stoesser T (2016) A local mesh refinement approach for large-eddy simulations of turbulent flows. *Int J Numer Methods Fluids* 82:261–285
29. Nicoud F, Ducros F (1999) Subgrid-scale stress modelling based on the square of the velocity gradient tensor. *Flow, Turbul Combust* 62:183–200
30. Huang S, Li Q (2010) A new dynamic one-equation subgrid-scale model for large eddy simulations. *Int J Numer Methods Eng* 81:835–865
31. Martin S, Bhushan B (2014) Fluid flow analysis of a shark-inspired microstructure. *J Fluid Mech* 756:5–29
32. Bixler GD, Bhushan B (2013) Shark skin inspired low-drag micro-structured surfaces in closed channel flow. *J Colloid Interface Sci* 393:384–396
33. Martin S, Bhushan B (2016) Modeling and optimization of shark-inspired riblet geometries for low drag applications. *J Colloid Interface Sci* 474:206–215
34. Al-fahham MAH, Bigot S, Medina AV (2016) A study of fluid flow characteristics using micro structured surfaces produced by WEDM. Proceedings of 4M/IWMF Conference, 708, Lyngby, Denmark.
35. Martinez-Zavala H, Bhaduri D, Valera-Medina A, Bigot S (2019) Experimental study on heat transfer enhancement during condensation using microstructured surfaces. *Int. Conf. Appl. Energy, Västerås, Sweden.*
36. Quetzeri-Santiago MA, Yokoi K, Castrejón-Pita AA, Castrejón-Pita JR (2019) Role of the dynamic contact angle on splashing. *Phys Rev Lett* 122(22):228001
37. Stalder AF, Kulik G, Sage D, Barbieri L, Hoffmann P (2006) A snake-based approach to accurate determination of both contact points and contact angles. *Colloids Surfaces A: Physicochem Eng Asp* 286(1–3):92–103
38. Stalder AF, Melchior T, Muller M, Sage D, Blu T, Unser M (2010) Low-bond axisymmetric drop shape analysis for surface tension and contact angle measurements of sessile drops. *Colloids Surfaces A: Physicochem Eng Asp* 364(1–3):72–81
39. Cione JJ (2014) The relative roles of the ocean and atmosphere as revealed by buoy air–sea observations in hurricanes. *Mon Weather Rev* 143:904–913
40. Fu YF, Yuan CQ, Bai XQ (2017) Marine drag reduction of shark skin inspired riblet surfaces. *Biosurface and Biotribology* 3:11–24
41. Schlichting H (2000) *Boundary layer theory*, 8th edn. Springer-Verlag, Berlin Heidelberg
42. Bechert DW, Bruse M, Hage W, Van Der Hoeven JGT, Hoppe G (1997) Experiments on drag-reducing surfaces and their optimization with an adjustable geometry. *J Fluid Mech* 338:59–87
43. Chatterjee A, Derby MM, Peles Y, Jensen MK (2014) Enhancement of condensation heat transfer with patterned surfaces. *Int J Heat Mass Transf* 71:675–681
44. Wen R, Xu S, Zhao D, Lee YC, Ma X, Yang R (2017) Hierarchical superhydrophobic surfaces with micropatterned nanowire arrays for high-efficiency jumping droplet condensation. *ACS Appl Mater Interfaces* 9:44911–44921
45. Ghosh A, Beaini S, Zhang BJ, Ganguly R, Megaridis CM (2014) Enhancing dropwise condensation through bioinspired wettability patterning. *Langmuir* 30(43):13103–13115
46. Mahapatra PS, Ghosh A, Ganguly R, Megaridis CM (2016) Key design and operating parameters for enhancing dropwise condensation through wettability patterning. *Int J Heat Mass Transf* 92:877–883
47. Anand S, Rykaczewski K, Bengaluru Subramanyam S, Beysens D, Varanasi KK (2015) How droplets nucleate and grow on liquids and liquid impregnated surfaces. *Soft Matter* 11:69–80
48. Grooten MH, Geld CW (2010) The importance of drainage in dropwise condensation from flowing air–steam mixtures. Proceedings of the 14th Int. Heat Transf. Conf., Washington, USA, 51–60.
49. He M, Zhang Q, Zeng X, Cui D, Chen J, Li H, Wang J, Song Y (2013) Hierarchical porous surface for efficiently controlling microdroplets' self-removal. *Adv Mater* 25(16):2291–2295

Publisher's Note Springer Nature remains neutral with regard to jurisdictional claims in published maps and institutional affiliations.